XL CILAMCE
IBERO-LATIN AMERICAN CONGRESS ON COMPUTATIONAL METHODS IN ENGINEERING
NOVEMBER 11-14, 2019
Praiamar Natal Hotel & Convention
Natal, RN-BRAZIL

Development of a procedure for the solution of non-homogeneous partial differential equations using the Scaled Boundary Finite Element Method

Karolinne O. Coelho
Philippe R. B. Devloo
karolinneoc@gmail.com
phil@unicamp.br
Computational Mechanics Laboratory, University of Campinas (LabMeC/UNICAMP). Rua Josiah Willard Gibbs, 85, 13083-839, Campinas/São Paulo, Brazil.

Abstract. The Scaled Boundary Finite Element Method (SBFEM) is a finite element approximation technique in which the shape functions are constructed based on a semi-analytical approach. Due to its features, this method is particularly efficient to approximate problems with strong internal singularities, for instance, fracture mechanics simulation. The main focus of this study is to analyze the approximation properties of SBFEM and use them to develop a procedure to approximate non-homogeneous partial differential equations (PDEs). It was observed optimal rates of convergence for problems with square-root singularity. Furthermore, the orthogonality between SBFEM approximation at the boundary and the internal bubble functions, which represent the non-homogeneous term, is observed. Such a property is applied to extend the SBFEM to approximate non-homogeneous PDEs with internal polynomial functions. Rates of convergence are computed to demonstrate the effectiveness of this technique.

Keywords: SBFEM, body loads, square-root singularity, fracture mechanics.

1 Introduction

When a physical problem is described by an ordinary differential equation (ODE), classical mathematical techniques can, in certain cases, lead to the analytical solution. For instance, when there is symmetry for the PDE, it can be rewritten in terms of one variable and then its solution is written analytically. For take advantage of this feature, even for general cases with no symmetry, it can be used a different coordinate system, for example, with radial and tangential coordinates [1].

The scaled boundary technique uses the radial and tangential coordinates to scale the boundary of a domain. In such a technique, the element's boundary is scaled from the centre with a dimensionless radial coordinate ξ, which varies from 0, at the scaling centre, to 1, at the boundary. The SBFEM (Scaled Boundary Finite Element Method) applies the scaled boundary technique in finite elements leading to a semi-analytical solution.

SBFEM is defined as a finite element approximation in which the shape functions are constructed based on a semi-analytical approach [2]. The boundary of a SBFEM element is discretized with isoparametric surface finite elements (where the coordinates are $-1 \leq \eta \leq 1$ and $-1 \leq \zeta \leq 1$, for 3D elements). Thus, the radial coordinate ξ, in addition to the surface coordinates, η and ζ, generates the scaled boundary coordinates system. Due to the features of the SBFEM element, the geometric transformation between the Cartesian and scaled boundary coordinates is unique. This coordinate system transformation is named the scaled boundary transformation.

In SBFEM meshes, the domain is discretized in polygons in which the only requirement is that a specific point (named scaling centre) can be visible for all the boundary. This type of polygon is known as S-domain [2] (see Fig. 1). An S-element is an S-domain in which the boundary is discretized with standard FEM isoparametric formulations. Inside an S-element, the solution is semi-analytical.

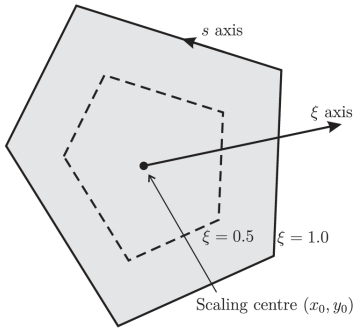

Figure 1. SBFEM polygon and its coordinates (s is the tangential and ξ is the radial coordinate).

The features of SBFEM make this method particularly efficient to approximate problems with strong internal singularities, for instance, fracture mechanics simulation [3]. Another application is in the simulation of unbounded domains [4]. Moreover, the compatibility of SBFEM with FEM allows the coupling between FEM and SBFEM meshes. However, for approach of non-homogeneous PDEs, SBFEM leads to complex approximations [5]. Also, the implementation of SBFEM in FEM codes can be simplified if the geometric map of a collapsed element is applied instead of the scaled boundary transformation.

Therefore, this study aims to analyze the properties of the SBFEM approach and use them to develop a procedure to approximate non-homogeneous partial differential equations (PDEs). The proposed methodology was implemented in C++, in an object-oriented finite element library, the NeoPZ. For this purpose, the SBFEM formulation is applied into a collapsed isoparametric element. Such an approach avoids the scaled boundary transformation, which is useful for SBFEM implementation on FE codes.

In section 2 a brief of the main equations of the SBFEM formulation is presented. Section 3 proves that the coefficient matrices of an SBFEM element can be computed by using a collapsed finite element. In the following, it is developed an enriched functional space for a general SBFEM approximation based on internal polynomial functions (section 4). Such a functional space is applied to approach problems

with non-homogeneous PDEs (for instance, body loads) and has the feature of fully orthogonality with SBFEM approximation at the boundary.

Three examples show the accuracy of the SBFEM approximation (section 5). Firstly, it is observed optimal rate of convergence for a problem with square-root singularity. For this example, it is shown that the eigenvalues of the SBFEM formulation converge to the Steklov eigenvalues. Subsequently, two examples with body loads (Poisson and elasticity problems) were evaluated. Optimal rates of convergence were also obtained for both L^2 and energy norm.

2 A brief introduction to the Scaled Boundary Finite Element Method

This section shows a brief of the fundamental equations for classical SBFEM formulation. For more details, the authors recommend Song's work [2]. The starting point is solving the SBFEM equation in displacement, given by

$$\xi^2 \mathbf{E}_0 \mathrm{D}^2 \mathbf{u}(\xi) + \xi \left(\mathbf{E}_0 + \mathbf{E}_1^T - \mathbf{E_1} \right) \mathrm{D}\mathbf{u}(\xi) - \mathbf{E}_2 \mathbf{u}(\xi) = 0, \tag{1}$$

which is a second-order ordinary differential equation, where ξ is the independent variable and $\mathbf{u}(\xi)$ is the displacement field. The $\mathbf{E}_0$, $\mathbf{E}_1$, and $\mathbf{E}_2$ are the SBFEM coefficient matrices. They are obtained by geometric transformations for classical SBFEM approximations [2] and are expressed as

$$\mathbf{E}_0 = \int_{-1}^{+1} \mathbf{B}_1^T \mathbf{C} \mathbf{B}_1 |\mathbf{J}_b| \, \mathrm{d}\eta \tag{2}$$

$$\mathbf{E}_1 = \int_{-1}^{+1} \mathbf{B}_2^T \mathbf{C} \mathbf{B}_1 |\mathbf{J}_b| \, \mathrm{d}\eta \tag{3}$$

$$\mathbf{E}_2 = \int_{-1}^{+1} \mathbf{B}_2^T \mathbf{C} \mathbf{B}_2 |\mathbf{J}_b| \, \mathrm{d}\eta, \tag{4}$$

where $\mathbf{C}$ is the constitutive tensor, $\mathbf{B}_i$ matrices are given by,

$$\mathbf{B}_1 = \begin{bmatrix} \mathrm{D}\mathbf{y}_b & 0 \\ 0 & -\mathrm{D}\mathbf{x}_b \\ -\mathrm{D}\mathbf{x}_b & \mathrm{D}\mathbf{y}_b \end{bmatrix} \mathbf{N}(\eta) |\mathbf{J}_b| \tag{5}$$

$$\mathbf{B}_2 = \begin{bmatrix} -\mathbf{y}_b & 0 \\ 0 & \mathbf{x}_b \\ \mathbf{x}_b & -\mathbf{y}_b \end{bmatrix} \mathbf{N}'(\eta) |\mathbf{J}_b|, \tag{6}$$

and $\mathbf{N}(\eta)$ is a matrix with the shape functions and $|\mathbf{J}_b|$ is the determinant of the Jacobian matrix.

The ODE (Eq. 1) is solved through a system of first-order differential equations. For this purpose, two relationships between the displacement field and the force vector, obtained from the application of the virtual work principle in scaled boundary coordinates, are expressed as

$$\mathbf{q}(\xi) = \xi \mathbf{E}_0 \mathrm{D}\mathbf{u}(\xi) + \mathbf{E}_1^T \mathbf{u}(\xi) \tag{7}$$

$$\xi \mathrm{D}\mathbf{q}(\xi) = \xi \mathbf{E}_1 \mathrm{D}\mathbf{u}(\xi) + \mathbf{E}_2 \mathbf{u}(\xi), \tag{8}$$

where $\mathbf{q}(\xi)$ is the force vector.

The second-order ODE (Eq. 1) is solved through a system of first-order ODEs. The first equation is obtained isolating $\mathrm{D}\mathbf{u}(\xi)$ from Eq. 7, as follows

$$\xi \mathrm{D}\mathbf{u}(\xi) = \mathbf{E}_0^{-1}\mathbf{q}(\xi) - \mathbf{E}_0^{-1}\mathbf{E}_1^T\mathbf{u}(\xi). \tag{9}$$

The second equation is obtained by substitution of $\mathrm{D}^2\mathbf{u}(\xi)$ (obtained by differentiation of Eq. 9) and substituting it into Eq. 1, resulting in

$$\xi \mathrm{D}\mathbf{q}(\xi) = \xi \mathbf{E_1} \mathrm{D}\mathbf{u}(\xi) + \mathbf{E}_2\mathbf{u}(\xi). \tag{10}$$

Replacing Eq. 9 into Eq. 10,

$$\xi \mathrm{D}\mathbf{q}(\xi) = \left(-\mathbf{E}_1\mathbf{E}_0^{-1}\mathbf{E}_1^T\mathbf{u}(\xi) + \mathbf{E}_2\mathbf{u}(\xi)\right) + \mathbf{E}_0\mathbf{E}_1^{-1}\mathbf{q}(\xi). \tag{11}$$

The system is composed of the Eq. 9 and 11, which can be grouped in a matrix form as follows:

$$\xi \left(\mathrm{D}\mathbf{X}(\xi)\right) = \mathbf{Z}_p\mathbf{X}(\xi), \text{ in } \Omega \tag{12}$$

$$\mathbf{X}(\xi = 1) = \begin{bmatrix} \mathbf{u}_0 \\ \mathbf{f}_0 \end{bmatrix}, \text{ in } \partial\Omega, \tag{13}$$

where:

$$\mathbf{Z}_p = \begin{bmatrix} -\mathbf{E}_0^{-1}\mathbf{E}_1^T & \mathbf{E}_0^{-1} \\ \mathbf{E_2} - \mathbf{E}_1\mathbf{E}_0^{-1}\mathbf{E}_1^T & \mathbf{E}_1\mathbf{E}_0 \end{bmatrix}, \tag{14}$$

$$\mathbf{X}(\xi) = \begin{bmatrix} \mathbf{u}(\xi) \\ \mathbf{q}(\xi) \end{bmatrix}. \tag{15}$$

The general solution to this type of linear system is well known as

$$\mathbf{X}(\xi) = \mathbf{c}\mathbf{\Phi}\xi^{\boldsymbol{\lambda}}, \tag{16}$$

that can be replaced in the Eq. 12:

$$\begin{aligned} \xi\left[\mathrm{D}\left(\mathbf{c}\mathbf{\Phi}\xi^{\boldsymbol{\lambda}}\right)\right] &= \mathbf{Z}_p\left(\mathbf{c}\mathbf{\Phi}\xi^{\boldsymbol{\lambda}}\right) \\ \lambda\mathbf{\Phi} &= \left(\mathbf{Z}_p - \boldsymbol{\lambda}\mathbf{I}\right), \end{aligned} \tag{17}$$

which is an eigenvalue problem, where $\boldsymbol{\lambda}$ is a vector with the eigenvalues and $\mathbf{\Phi}$ is a matrix with its respective eigenvectors. The eigenvectors are disposed of as a block matrix, as follows:

$$\mathbf{\Phi} = \begin{bmatrix} \mathbf{\Phi}_{un} & \mathbf{\Phi}_{up} \\ \mathbf{\Phi}_{qn} & \mathbf{\Phi}_{qp} \end{bmatrix}. \tag{18}$$

where $\mathbf{\Phi}_u$ is a block related to the displacement modes and, analogously, $\mathbf{\Phi}_q$ is the block related to the force modes.

Once $\mathbf{Z}_p$ is a Hamiltonian matrix, the eigenvalues $\boldsymbol{\lambda}$ occur in pairs. Therefore, the vector is divided into two parts, where the first one ($\boldsymbol{\lambda}_n$) is negative and the last part is its conjugate ($\boldsymbol{\lambda}_n = -\boldsymbol{\lambda}_p$). For a formulation for finite domains, considered in this paper, $\xi^{\boldsymbol{\lambda}}$ needs to be finite for $\xi = 0$ and then the negative values are applied. Otherwise, for infinite domains, the positive eigenvalues are utilized. Thus, the solution is written as:

$$\mathbf{u}(\xi) = \mathbf{\Phi}_{un}\xi^{\boldsymbol{\lambda}_n}\mathbf{c} \tag{19}$$

$$\mathbf{q}(\xi) = \mathbf{\Phi}_{qn}\xi^{\boldsymbol{\lambda}_n}\mathbf{c}, \tag{20}$$

where $\mathbf{c}$ is the integration constants, obtained by applying the boundary conditions, as follows:

$$\mathbf{c} = \mathbf{\Phi}_{un}^{-1}\mathbf{u}_b. \tag{21}$$

Therefore, we rewrite the solution of the ODE as:

$$\mathbf{u}(\xi) = \mathbf{\Phi}_{un}\xi^{\boldsymbol{\lambda}_n}\mathbf{\Phi}_{un}^{-1}\mathbf{u}_b. \tag{22}$$

The SBFEM solution of displacements is obtained interpolating the displacement function $\mathbf{u}(\xi)$ by the shape functions as follows

$$\mathbf{u}(\xi,\eta) = \mathbf{N}(\eta)\mathbf{\Phi}_{un}\xi^{\boldsymbol{\lambda}_n}\mathbf{\Phi}_{un}^{-1}\mathbf{u}_b, \tag{23}$$

where it can be identified the scaled boundary shape functions expressed as [6]

$$\Psi(\xi,\eta) = \mathbf{N}(\eta)\mathbf{\Phi}_{un}\xi^{\boldsymbol{\lambda}_n}\mathbf{\Phi}_{un}^{-1}. \tag{24}$$

3 Computation of SBFEM coefficient matrices using collapsed finite elements

In this section we show the proof that the geometric map of an SBFEM element's sector is obtained by using a standard quadrilateral element map where two nodes coincide. Such an element type is well-known as a collapsed finite element [7].

Consider a quadrilateral element with an arbitrary geometry at its left side as illustrated in Fig. 2 and corner nodes $\vec{\mathbf{x}}_i$.

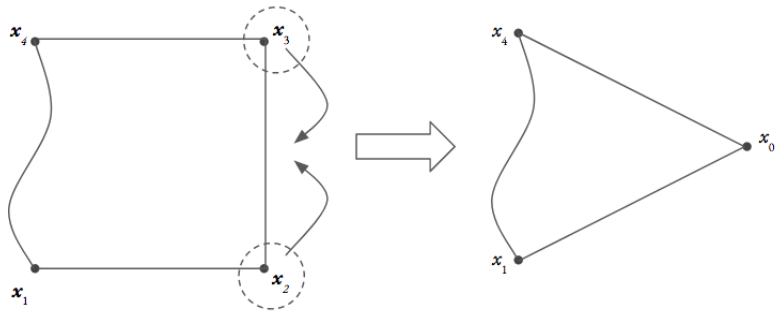

Figure 2. Geometric map for a SBFEM segment using geometry of collapsed finite elements.

Denote by $\vec{\mathbf{x}}_L(\eta) = \vec{\mathbf{x}}(-1,\eta)$ where $-1 \leq \eta \leq 1$ a nonlinear map when $\hat{\xi} \equiv -1$. Moreover, without lack of generality, we choose the side given by vertices $\vec{\mathbf{x}}_1$ and $\vec{\mathbf{x}}_4$. Then, the map satisfies $\vec{\mathbf{x}}_L(-1) = \vec{\mathbf{x}}_1,\ \vec{\mathbf{x}}_L(1) = \vec{\mathbf{x}}_4$. Applying transfinite mapping, the coordinate $\vec{\mathbf{x}}(\xi,\eta)$ of the quadrilateral element is computed as[1]:

$$\vec{\mathbf{x}}(\xi,\eta) = \vec{\mathbf{x}}_L(\eta)\frac{1-\hat{\xi}}{2} + \vec{\mathbf{x}}_2\frac{(1-\eta)(1-\hat{\xi})}{4} + \vec{\mathbf{x}}_3\frac{(1+\eta)(1-\hat{\xi})}{4}, \tag{25}$$

[1]Note that $\vec{\mathbf{x}}(\xi,\eta) = \begin{Bmatrix} x(\xi,\eta) \\ y(\xi,\eta) \end{Bmatrix}$ and $\vec{\mathbf{x}}_L(\xi,\eta) = \begin{Bmatrix} x_L(\xi,\eta) \\ y_L(\xi,\eta) \end{Bmatrix}$

where $(\hat{\xi}, \eta) \in]-1,1[\times]-1,1[$.

Consider $\eta = 0$ and take $\vec{\mathbf{x}}_0 \in [\vec{\mathbf{x}}_2, \vec{\mathbf{x}}_3]$. Collapsing this side, i.e. $\vec{\mathbf{x}}_2 = \vec{\mathbf{x}}_3 = \vec{\mathbf{x}}_0$ (see Fig. 2), the previous map becomes:

$$\vec{\mathbf{x}}(\hat{\xi}, \eta) = \vec{\mathbf{x}}_L(\eta)\frac{1+\hat{\xi}}{2} + \vec{\mathbf{x}}_0\frac{(1-\hat{\xi})}{2}. \tag{26}$$

The parametrization is modified ($\xi = (1+\hat{\xi})/2$) to change the variable domain for $0 \leq \xi \leq 1$. Then, the map is given by:

$$\vec{\mathbf{x}}(\xi, \eta) = \xi(\vec{\mathbf{x}}_L(\eta) - \vec{\mathbf{x}}_0) + \vec{\mathbf{x}}_0, \tag{27}$$

which corresponds to the SBFEM geometric map. This procedure is especially useful for implementing SBFEM in FEM codes since it implies that the standard geometric maps of finite elements can be used to compute the geometric SBFEM maps.

Subsequently, it is proved that $\mathbf{B}_1$ and $\mathbf{B}_2$ matrices can be obtained by the geometric transformation of collapsed finite elements. Although this proof is accomplished using the Laplacian equation, the steps can be applied for any partial differential equation.

Let $\mathbf{\Psi}$ be an approximation for the domain. Then,

$$\begin{aligned}\int_\Omega \nabla\Psi_i \cdot \nabla\Psi_j \, \mathrm{d}\Omega &= \int_{\hat{\Omega}} \nabla\Psi_i^T \nabla\Psi_j \, |\mathbf{J}| \, \mathrm{d}\xi\mathrm{d}\eta \\ &= \int_{\hat{\Omega}} \nabla_{\hat{\xi}\eta}\Psi_i^T \mathbf{J}^{-1}\mathbf{J}^{-T}\nabla_{\hat{\xi}\eta}\Psi_j \, |\mathbf{J}| \, \mathrm{d}\xi\mathrm{d}\eta,\end{aligned} \tag{28}$$

where $0 \leq \xi \leq 1$ and $-1 \leq \hat{\xi} \leq 1$.

Firstly Jacobian matrix is calculated using the geometric map (Eq. 25) as follows,

$$\begin{aligned}\mathbf{J} &= \nabla\vec{\mathbf{x}} \\ &= \begin{pmatrix} \dfrac{\partial x}{\partial\hat{\xi}} & \dfrac{\partial x}{\partial\eta} \\ \dfrac{\partial y}{\partial\hat{\xi}} & \dfrac{\partial y}{\partial\eta} \end{pmatrix} \\ &= \begin{pmatrix} \dfrac{x_L(\eta) - x_0}{2} & \dfrac{\partial x_L(\eta)}{\partial\eta}\dfrac{(1+\hat{\xi})}{2} \\ \dfrac{y_L(\eta) - y_0}{2} & \dfrac{\partial y_L(\eta)}{\partial\eta}\dfrac{(1+\hat{\xi})}{2} \end{pmatrix}.\end{aligned} \tag{29}$$

Applying the transformation $\hat{\xi} = 2\xi - 1$ to change the domain of parametrization results in

$$\begin{aligned}\mathbf{J} &= \begin{pmatrix} \dfrac{x_L(\eta) - x_0}{2} & \dfrac{\partial x_L(\eta)}{\partial\eta}\xi \\ \dfrac{y_L(\eta) - y_0}{2} & \dfrac{\partial y_L(\eta)}{\partial\eta}\xi \end{pmatrix} \\ &= \mathbf{J}_b \begin{pmatrix} 1 & 0 \\ 0 & \xi \end{pmatrix},\end{aligned} \tag{30}$$

where $\mathbf{J}_b$ is the Jacobian matrix at the boundary.

The Jacobian inverse is given by:

$$\mathbf{J}^{-1} = \frac{1}{|\mathbf{J}|}\begin{pmatrix} \dfrac{\partial y_L(\eta)}{\partial \eta}\xi & -\dfrac{\partial x_L(\eta)}{\eta}\xi \\ \dfrac{-y_L(\eta)+y_0}{2} & \dfrac{x_L(\eta)-x_0}{2} \end{pmatrix}, \tag{31}$$

where the determinant of a Jacobian transformation of a collapsed element is expressed as

$$|\mathbf{J}| = \xi|\mathbf{J}_b|. \tag{32}$$

Now consider that the approximation $\boldsymbol{\Psi}(\xi,\eta)$ is given by

$$\Psi(\xi,\eta) = \mathbf{f}(\xi)\boldsymbol{\psi}(\eta), \tag{33}$$

where $\mathbf{f}(\xi)$ is a function of ξ and $\boldsymbol{\psi}(\eta)$ is a vector with the finite elements shape functions.

Replacing Eqs. 31 and 33 in Eq. 28, the integrand of the Laplacian problem is expressed as

$$\begin{aligned}
\nabla\Psi_i^T\nabla\Psi_j = &\begin{Bmatrix} \mathbf{f}'(\xi)\boldsymbol{\psi}(\eta) \\ \mathbf{f}(\xi)\boldsymbol{\psi}'(\eta) \end{Bmatrix}^T \frac{1}{|\mathbf{J}|}\begin{pmatrix} \frac{\partial y_L(\eta)}{\partial\eta}\xi & -\frac{\partial x_L(\eta)}{\eta}\xi \\ \frac{-y_L(\eta)+y_0}{2} & \frac{x_L(\eta)-x_0}{2} \end{pmatrix}\frac{1}{|\mathbf{J}|}\begin{pmatrix} \frac{\partial y_L(\eta)}{\partial\eta}\xi & \frac{-y_L(\eta)+y_0}{2} \\ -\frac{\partial x_L(\eta)}{\eta}\xi & \frac{x_L(\eta)-x_0}{2} \end{pmatrix} \\
&\begin{Bmatrix} \mathbf{f}'(\xi)\boldsymbol{\psi}(\eta) \\ \mathbf{f}(\xi)\boldsymbol{\psi}'(\eta) \end{Bmatrix} \\
= &\begin{Bmatrix} \mathbf{f}'(\xi)\xi^{-1} \\ \mathbf{f}(\xi)\xi^{-1} \end{Bmatrix}^T \frac{1}{|\mathbf{J}_b|^2}\begin{pmatrix} \frac{\partial y_L(\eta)}{\partial\eta}\xi\boldsymbol{\psi}(\eta) & -\frac{\partial x_L(\eta)}{\eta}\xi\boldsymbol{\psi}(\eta) \\ \frac{-y_L(\eta)+y_0}{2}\boldsymbol{\psi}'(\eta) & \frac{x_L(\eta)-x_0}{2}\boldsymbol{\psi}'(\eta) \end{pmatrix} \\
&\begin{pmatrix} \frac{\partial y_L(\eta)}{\partial\eta}\xi\boldsymbol{\psi}(\eta) & \frac{-y_L(\eta)+y_0}{2}\boldsymbol{\psi}'(\eta) \\ -\frac{\partial x_L(\eta)}{\eta}\xi\boldsymbol{\psi}(\eta) & \frac{x_L(\eta)-x_0}{2}\boldsymbol{\psi}'(\eta) \end{pmatrix}\begin{Bmatrix} \mathbf{f}'(\xi)\xi^{-1} \\ \mathbf{f}(\xi)\xi^{-1} \end{Bmatrix}.
\end{aligned} \tag{34}$$

Both $\mathbf{B}_1$ and $\mathbf{B}_2$ SBFEM matrices are identified in Eq. 39. Therefore they are written as

$$\mathbf{B}_1 = \frac{1}{|\mathbf{J}_b|}\begin{pmatrix} \dfrac{\partial y_L(\eta)}{\partial\eta} \\ -\dfrac{\partial x_L(\eta)}{\partial\eta} \end{pmatrix}\boldsymbol{\psi}(\eta) \tag{35}$$

$$\mathbf{B}_2 = \frac{1}{|\mathbf{J}_b|}\begin{pmatrix} \dfrac{-y_L(\eta)+y_0}{2} \\ \dfrac{x_L(\eta)-x_0}{2} \end{pmatrix}\boldsymbol{\psi}'(\eta), \tag{36}$$

where $\mathbf{B}_1$ and $\mathbf{B}_2$ has dimensions $2\times n$ for a 2D element, and n is the number of shape functions.

Similarly, the same principle can be applied to three-dimensional maps used in SBFEM by collapsing 4 nodes of a hexahedral element (for a 4 noded face) or by collapsing 3 nodes of a prism (for a 3 noded face)[2].

Generically, we define functions for d dimensional elements, on each side of the SBFEM element. The functions that compose $\mathbf{B}_i$ can be divided into two sets of d dimensional shape functions, according to the Jacobian inverse. These functions, written as $\boldsymbol{\phi}_1^d$ and $\boldsymbol{\phi}_2^d$, given by Eqs. 37 and Eq. 38, have the properties shown in Table 1.

$$\boldsymbol{\phi}_1^d = \frac{1+\xi}{2}\boldsymbol{\phi}^{d-1}(\eta) \tag{37}$$

[2] η stands for the lower-dimensional parameters. In three dimensions η is bidimensional.

$$\boldsymbol{\phi}_2^d = \frac{1-\xi}{2}\boldsymbol{\phi}^{d-1}(\eta) \tag{38}$$

Table 1. Volume shape functions derived from side shape functions , i.e. boundary shape functions.

	$\boldsymbol{\phi}_i^d(\xi=1)$	$\left.\frac{\partial \boldsymbol{\phi}_i^d}{\partial \xi}\right\vert_{\xi=1}$	$\left.\frac{\partial \boldsymbol{\phi}_i^d}{\partial \eta}\right\vert_{\xi=1}$
Set 1	$\boldsymbol{\phi}^{d-1}$	$\frac{\boldsymbol{\phi}^{d-1}}{2}$	$\frac{\partial \boldsymbol{\phi}^{d-1}}{\partial \eta}$
Set 2	$\mathbf{0}$	$-\frac{\boldsymbol{\phi}^{d-1}}{2}$	$\mathbf{0}$

These functions are used to compute $\mathbf{B}_i$ matrices, where the derivatives in Set 1 compose $\mathbf{B}_1$ and, similarly, $\mathbf{B}_2$ is given by derivatives of Set 2. The substitution of both $\mathbf{B}_1$ and $\mathbf{B}_2$ (Eqs. 35 and 36, respectively) into the integral (Eq. 28) results in

$$\int_\Omega \nabla\Psi_i \cdot \nabla\Psi_j \,\mathrm{d}\Omega = \int_0^1 \begin{Bmatrix} \mathbf{f}'(\xi)\xi^{-1} \\ \mathbf{f}(\xi)\xi^{-1} \end{Bmatrix}^T \begin{pmatrix} \mathbf{B}_1^T\xi \\ \mathbf{B}_2^T \end{pmatrix} \begin{pmatrix} \mathbf{B}_1\xi & \mathbf{B}_2 \end{pmatrix} \begin{Bmatrix} \mathbf{f}'(\xi)\xi^{-1} \\ \mathbf{f}(\xi)\xi^{-1} \end{Bmatrix} |\mathbf{J}|\mathrm{d}\xi. \tag{39}$$

Evaluating Eq. 39, the integral can be written in terms of $\mathbf{E}_0$, $\mathbf{E}_1$ and $\mathbf{E}_2$:

$$\begin{aligned} \int_\Omega \nabla\Psi_i \cdot \nabla\Psi_j \,\mathrm{d}\xi\mathrm{d}\eta &= \int_0^1 \begin{Bmatrix} \mathbf{f}'(\xi)\xi^{-1} \\ \mathbf{f}(\xi)\xi^{-1} \end{Bmatrix}^T \begin{pmatrix} \mathbf{B}_1^T\mathbf{B}_1\xi^2 & \mathbf{B}_1^T\mathbf{B}_2\xi \\ \mathbf{B}_2^T\mathbf{B}_1\xi & \mathbf{B}_2^T\mathbf{B}_2 \end{pmatrix} \begin{Bmatrix} \mathbf{f}'(\xi)\xi^{-1} \\ \mathbf{f}(\xi)\xi^{-1} \end{Bmatrix} |\mathbf{J}|\,\mathrm{d}\xi \\ &= \int_0^1 \begin{Bmatrix} \mathbf{f}'(\xi)\xi^{-1} \\ \mathbf{f}(\xi)\xi^{-1} \end{Bmatrix}^T \begin{pmatrix} \mathbf{E}_0\xi^2 & \mathbf{E}_1^T\xi \\ \mathbf{E}_1\xi & \mathbf{E}_2 \end{pmatrix} \begin{Bmatrix} \mathbf{f}'(\xi)\xi^{-1} \\ \mathbf{f}(\xi)\xi^{-1} \end{Bmatrix} |\mathbf{J}|\,\mathrm{d}\xi. \end{aligned} \tag{40}$$

Eq. 40 shows that the SBFEM coefficient matrices $\mathbf{E}_i$ can be obtained directly from traditional integration point contributions of either bidimensional or tridimensional partial differential equations using collapsed finite elements.

4 Construction of functional space for SBFEM approximations

The solution of the nonhomogeneous ODE can be decomposed into two parts as

$$\mathbf{X}(\xi) = \mathbf{X}_h(\xi) + \mathbf{X}_{nh}(\xi), \tag{41}$$

where $\mathbf{X}_h(\xi)$ is the SBFEM solution for null body loads (complementary or homogeneous solution) and $\mathbf{X}_{nh}$ is the particular solution, composed of bubble functions (or nonhomogeneous solution).

Firstly the general functional space for SBFEM approximations is defined. Afterward, the definition of both homogeneous and particular solutions is presented.

Definition 1. General functional space for SBFEM. Let V be a functional space for general SBFEM approximations. Then

$$V = \sum \xi^{\mathbf{s}_k}\mathbf{p}_k(\eta), \tag{42}$$

where $\mathbf{s}_k \in \mathbb{Q}$ and $\mathbf{p}_k$ is a vector space.

The general functional space for SBFEM has an important property that allows the construction of its space. Such a property, based on the construction of the general solution (Eq. 41), establishes that V can be written as a direct sum of two functional subspaces adequately chosen.

Proposition 1. Decomposition of the functional space for SBFEM. Let V^{sb} be the functional space for SBFEM with vanish body loads and V^0 is the space of bubble functions. Then, the functional space for SBFEM can be decomposed as:

$$V = V^{sb} \oplus V^0, \tag{43}$$

i.e. a direct sum of both spaces V^{sb} and V^0.

The functional subspaces V^{sb} and V^0 have relevant features. Both are defined in the following.

Definition 2. Functional space for homogeneous SBFEM solution. Let

$$\beta_V^{sb} = \{(\lambda_i, \boldsymbol{\phi}_i)\}, \tag{44}$$

be the basis of SBFEM approximation spaces, composed by eigenvalues and eigenvectors obtained by the solution of the eigenvalue problem ($\xi \mathbf{D}\mathbf{X}(\xi) = \mathbf{Z}_p\mathbf{X}(\xi)$). Then

$$V^{sb} = \text{span } (\beta_V^{sb}), \tag{45}$$

is the SBFEM approximation space for homogeneous equations.

Definition 3. Bubble functional spaces for SBFEM equations. Let V^0 be the bubble functional spaces for SBFEM equations, which is a subspace of V. Then we can write:

$$V^0 = \{\psi \in V \mid \psi|_{\partial\Omega} = 0\}, \tag{46}$$

where ψ is either polynomial or rational bubble functions, which construction follows a specific methodology, shown in topic 3.1.

Bubble functions are often applied to build enriched spaces [8]. In the present study, this space is applied to enrich the SBFEM functional space of homogeneous solutions to approximate non-homogeneous PDE. In other words, ψ approximate the particular solution $\mathbf{X}_{nh}$ of Eq. 41.

An important feature is the orthogonality between bubble functional space and homogeneous SBFEM space. This characteristic is described as a property in the following.

Proposition 2. Orthogonality of SBFEM subspaces. Let $V^{sb} \in V$ and $V^0 \in V$. Then, $V^{sb} \perp V^0$, i.e.,

$$\int_\Omega \nabla V^{sb} \cdot \nabla V^0 \mathrm{d}\Omega = 0. \tag{47}$$

It is worth mentioning that the choice of this functional space is explained by its relevant features. Firstly, this space can be enriched to achieve an optimal rate of convergence. Secondly, due to its orthogonality, the approach can be divided into interior and exterior (boundary) problem, which can be solved separately.

4.1 Construction of bubble functions

The construction of bubble functional space is accomplished by building polynomial and rational bubble functions. It is important to mention that the rational basis is composed of the standard SBFEM functions. The construction process is quite different from the traditional bubble function approach and it is one of the contributions for the method.

Generally, the bubble functions are constructed as a linear combination of basis function ψ_k^e, as follows

$$\psi(\xi,\eta) = \psi_q(\xi) + \sum_{k=1}^{N} \psi_k(\xi)$$
$$= \sum_e \psi_q^e(\xi) + \sum_{k=1}^{N} \sum_e \psi_k^e(\xi), \tag{48}$$

where $\psi_q^e(\xi)$ is a rational bubble function and $\psi_k^e(\xi)$ is the k-th order basis function of a sector covered by the scaling center, which is given by:

$$\psi_k^e = \sum_{i=1}^{k+1} N_i(\eta) f_k(\xi), \tag{49}$$

where $f_k(\xi)$ is a polynomial or a rational function adequately chosen.

In order to illustrate the construction of a base function, let $\psi(\xi,\eta)$ represent a quadratic bubble function. Then,

$$\psi(\xi,\eta) = \sum_e \psi_1^e(\xi) + \psi_2^e(\xi), \tag{50}$$

where $\psi(0,\eta) = 1$ and $\psi(1,\eta) = 0$. For the linear case, $f_i(\xi)$ is chosen as

$$f_1(\xi) = (1-\xi). \tag{51}$$

Then, according to Eq. 50,

$$\psi_1^e(\xi,\eta) = \frac{1-\eta}{2}(1-\xi) + \frac{1+\eta}{2}(1-\xi), \tag{52}$$

which is shown in Fig. 3(a).

In order to obey the partition of unity, quadratic basis function are nil in both boundary and scaling centre ($\psi_2(0,\eta) = 0$ and $\psi_2(1,\eta)$ = 0). Thus, $f_2(\xi)$ can be written as

$$f_2(\xi) = (\xi - \xi^2). \tag{53}$$

Consequently, its respective basis ψ_2^e is given by

$$\psi_2^e(\xi,\eta) = \frac{(1-\eta)}{2}(\xi-\xi^2) + \frac{(1+\eta)}{2}(\xi-\xi^2) + \frac{(1+\eta)(1-\eta)}{2}(\xi-\xi^2), \tag{54}$$

which is plotted in Fig. 3(b).

Lastly, the sum of both linear and quadratic basis (Eq. 50) leads to the quadratic bubble function, as shown in Fig. 3(c).

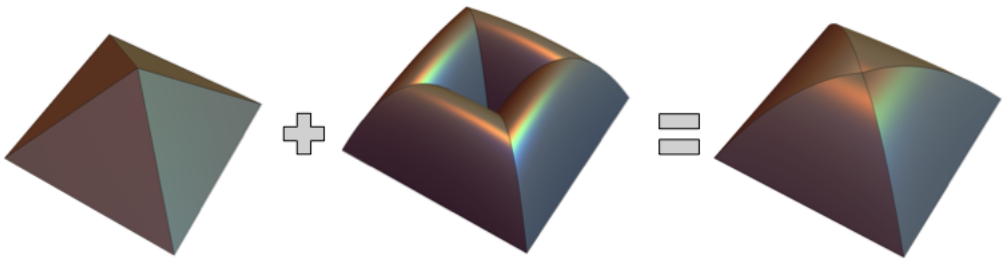

(a) Hat function (b) Quadratic Function (c) Bubble function

Figure 3. Composition of a bubble function.

For high order elements, the same strategy is applied, i.e. polynomial functions that are nil in both boundary and scaling centre are constructed, as in the following:

$$\psi_k^e = \sum_{i=1}^{k+1} N_i(\eta)(\xi - \xi^n). \tag{55}$$

In spite of the good accuracy, if the functional space is composed only of polynomial functions, poor rates of convergence would be obtained. In other words, a polynomial space of bubble functions does not achieve optimum rates of convergence for the SBFEM approach. Examples evaluated with only polynomial bubble functions leads to rates of convergence equal to 1 and 2, respectively for energy and L^2 error norm. More details of this result can be seen in section 5, in the second example. It is a result of a poor functional space, which suggests that more functions are needed to complete the V^0 space.

Low rates of convergence occur because the polynomial functions are not sufficient to cancel the influence of the rational functions at the element's domain. For this purpose, V^0 must also be enriched with adequate rational functions, specifically the ones that compose the boundary functional basis. In other words, the rational bubble functions formed are given by

$$\psi_q^e = \sum_{i=1}^{k+1} N_i(\eta)\phi_j(\xi - \xi^{\lambda_j}), \tag{56}$$

where ϕ_j is the eigenvector related to the eigenvalue λ_j.

With the complete bubble functional space, optimum rates of convergence were obtained ($p+1$ for L^2 error norm and p for energy error norm, with p equal to the polynomial order), as presented in the topic 5, higher than in other studies [9, 10]. The approximation of the particular solution, obtained with bubble functions, is applied to calculate stiffness matrix and body loads vector. Both formulations are deduced in the following.

4.2 Stiffness matrix

For the computation of the stiffness matrix, the starting point is to evaluate the virtual strain energy equation (from the virtual work principle) and replace the constitutive relationship and the strain field. These equations are the same used in standard SBFEM solution procedure for the virtual work principle, constitutive law, and strain field, respectively. Thus, the virtual strain energy is given by

$$\begin{aligned} U_\epsilon &= \int_\Omega \delta\boldsymbol{\epsilon}^T \mathbf{C}\boldsymbol{\epsilon}\, \mathrm{d}\Omega_e \\ &= \int_0^1 \int_{-1}^{+1} \xi \mathrm{D}\delta\mathbf{u}(\xi)^T \mathbf{B}_1^T \mathbf{C}\mathbf{B}_1 \mathrm{D}\mathbf{u}(\xi) + \delta\mathbf{u}(\xi)^T \mathbf{B}_2^T \mathbf{C}\mathbf{B}_1 \mathrm{D}\mathbf{u}(\xi) + \mathrm{D}\delta\mathbf{u}(\xi)^T \mathbf{B}_1^T \mathbf{C}\mathbf{B}_2 \mathbf{u}(\xi) \\ &+ \frac{1}{\xi}\delta\mathbf{u}(\xi)^T \mathbf{B}_2^T \mathbf{C}\mathbf{B}_2 \mathbf{u}(\xi)\, \mathrm{d}\xi. \end{aligned} \tag{57}$$

Replacing the SBFEM coefficient matrices (Eq. 2, 3 and 4) into Eq. 57:

$$U_\epsilon = \int_0^1 \mathrm{D}\delta\mathbf{u}(\xi)^T \mathbf{E}_0 \mathrm{D}\mathbf{u}(\xi)\xi + \delta\mathbf{u}(\xi)^T \mathbf{E}_1^T \mathrm{D}\mathbf{u}(\xi) + \mathrm{D}\delta\mathbf{u}(\xi)^T \mathbf{E}_1 \mathbf{u}(\xi) + \frac{1}{\xi}\delta\mathbf{u}(\xi)^T \mathbf{E}_2 \mathbf{u}(\xi)\, \mathrm{d}\xi. \tag{58}$$

The solution postulated for $\mathbf{u}(\xi)$ is given by

$$\mathbf{u}(\xi) = \boldsymbol{\Psi}\xi^{\boldsymbol{\Lambda}}\boldsymbol{\Psi}^{-1}\mathbf{u}_b, \tag{59}$$

where

$$\boldsymbol{\Psi} = \begin{bmatrix} \boldsymbol{\Phi}_{un} & \boldsymbol{\psi} \end{bmatrix}, \tag{60}$$

and

$$\boldsymbol{\Lambda} = \text{diag}\left(\begin{Bmatrix} -\boldsymbol{\lambda}_{un} & \boldsymbol{\lambda}_0 \end{Bmatrix} \right), \tag{61}$$

$\boldsymbol{\Phi}_{un}$ is the eigenvector matrix and $\boldsymbol{\lambda}_{un}$ its respective eigenvalues, and $\boldsymbol{\psi}$ is the matrix that composes the basis of bubble functions with its respective exponents $\boldsymbol{\lambda}_0$. Moreover, $\boldsymbol{\lambda}_{un}$ are the negative eigenvalues. Substituting $\mathbf{u}(\xi)$ into Eq. 58:

$$\begin{aligned} U_\epsilon = \int_0^1 & \left(\boldsymbol{\Psi}^T \text{diag}(\boldsymbol{\Lambda}) \xi^{\boldsymbol{\Lambda}-1} \boldsymbol{\Psi}^{-T}\right) \mathbf{E}_0 \left(\boldsymbol{\Psi}^{-1} \text{diag}(\boldsymbol{\Lambda}) \xi^{\boldsymbol{\Lambda}-1} \boldsymbol{\Psi} \xi \ \mathbf{u}_b\right) \\ & + \left(\boldsymbol{\Psi}^T \xi^{\boldsymbol{\Lambda}} \boldsymbol{\Psi}^{-T}\right) \mathbf{E}_1^T \left(\boldsymbol{\Psi}^{-1} \text{diag}(\boldsymbol{\Lambda}) \xi^{\boldsymbol{\Lambda}-1} \boldsymbol{\Psi} \ \mathbf{u}_b\right) \\ & + \left(\boldsymbol{\Psi}^T \text{diag}(\boldsymbol{\Lambda}) \xi^{\boldsymbol{\Lambda}-1} \boldsymbol{\Psi}^{-T}\right) \mathbf{E}_1 \left(\boldsymbol{\Psi}^{-1} \xi^{\boldsymbol{\Lambda}} \boldsymbol{\Psi} \ \mathbf{u}_b\right) + \left(\boldsymbol{\Psi}^T \xi^{\boldsymbol{\Lambda}} \boldsymbol{\Psi}^{-T}\right) \mathbf{E}_2 \left(\boldsymbol{\Psi}^{-1} \xi^{\boldsymbol{\Lambda}} \boldsymbol{\Psi} \ \mathbf{u}_b\right) \ \mathrm{d}\xi. \end{aligned} \tag{62}$$

Then, the stiffness matrix has the form

$$\begin{aligned} \mathbf{K} = \int_0^1 & \boldsymbol{\Psi}^T \text{diag}(\boldsymbol{\Lambda}) \xi^{\boldsymbol{\Lambda}-1} \left(\boldsymbol{\Psi}^{-T} \mathbf{E}_0 \boldsymbol{\Psi}^{-1}\right) \text{diag}(\boldsymbol{\Lambda}) \xi^{\boldsymbol{\lambda}-1} \boldsymbol{\Psi} \xi + \boldsymbol{\Psi}^T \xi^{\boldsymbol{\Lambda}} \left(\boldsymbol{\Psi}^{-T} \mathbf{E}_1^T \boldsymbol{\Psi}^{-1}\right) \text{diag}(\boldsymbol{\Lambda}) \xi^{\boldsymbol{\Lambda}-1} \boldsymbol{\Psi} \\ & + \boldsymbol{\Psi}^T \text{diag}(\boldsymbol{\Lambda}) \xi^{\boldsymbol{\Lambda}-1} \left(\boldsymbol{\Psi}^{-T} \mathbf{E}_1 \boldsymbol{\Psi}^{-1}\right) \xi^{\boldsymbol{\Lambda}} \boldsymbol{\Psi} + \boldsymbol{\Psi}^T \xi^{\boldsymbol{\Lambda}} \left(\boldsymbol{\Psi}^{-T} \mathbf{E}_2 \boldsymbol{\Psi}^{-1}\right) \xi^{\boldsymbol{\Lambda}} \boldsymbol{\Psi} \ \mathrm{d}\xi, \end{aligned} \tag{63}$$

which can be rewritten as:

$$\mathbf{K} = \boldsymbol{\Psi}^{-T} \mathbf{K}_{exp} \boldsymbol{\Psi}^{-1}, \tag{64}$$

where:

$$\begin{aligned} \mathbf{K}_{exp} = \int_0^1 & \boldsymbol{\Psi}^T \text{diag}(\boldsymbol{\Lambda}) \xi^{\boldsymbol{\Lambda}-1} \mathbf{E}_0 \text{diag}(\boldsymbol{\Lambda}) \xi^{\boldsymbol{\Lambda}-1} \boldsymbol{\Psi} \xi + \boldsymbol{\Psi}^T \xi^{\boldsymbol{\Lambda}} \mathbf{E}_1^T \text{diag}(\boldsymbol{\Lambda}) \xi^{\boldsymbol{\Lambda}-1} \boldsymbol{\Psi} \\ & + \boldsymbol{\Psi}^T \text{diag}(\boldsymbol{\Lambda}) \xi^{\boldsymbol{\Lambda}-1} \mathbf{E}_1 \xi^{\boldsymbol{\Lambda}} \boldsymbol{\Psi} + \boldsymbol{\Psi}^T \xi^{\boldsymbol{\Lambda}} \mathbf{E}_2 \xi^{\boldsymbol{\Lambda}} \boldsymbol{\Psi} \ \mathrm{d}\eta \mathrm{d}\xi. \end{aligned} \tag{65}$$

Indeed, due to the orthogonality of the functional space, the stiffness matrix can be decomposed as:

$$\mathbf{K} = \begin{pmatrix} \mathbf{K}^{sb} & \mathbf{0} \\ \mathbf{0} & \mathbf{K}^0 \end{pmatrix}. \tag{66}$$

where $\mathbf{K}^{sb}$ is the SBFEM stiffness matrix, and $\mathbf{K}_0$ is the bubble stiffness matrix. As a result, an SBFEM approximation with body loads can be decoupled into boundary and domain problems. The proposed approximation for body forces simplifies the calculations and is computationally efficient.

4.3 Body loads approximation

Consider the virtual work principle, specifically the virtual work due to external forces, specifically the part related to the body loads. Then, using Eq. 59 leads to

$$\begin{aligned} \int_{\Omega_e} \delta \mathbf{u}^T \mathbf{f}(\xi, \eta) \mathrm{d}\Omega_e &= \int_0^1 \int_{-1}^{+1} \boldsymbol{\Psi}^{-T} \xi^{\boldsymbol{\Lambda}} \boldsymbol{\Psi}^T \mathbf{N}(\eta)^T \mathbf{f}(\xi, \eta) \xi |\mathbf{J}_b| \ \mathrm{d}\eta \ \mathrm{d}\xi \\ &= \boldsymbol{\Psi}^{-T} \mathbf{f}_{int}, \end{aligned} \tag{67}$$

where $\mathbf{f}_{int}$ is given by

$$\mathbf{f}_{int} = \int_0^1 \int_{-1}^{+1} \xi^{\mathbf{\Lambda}} \mathbf{\Psi}^T \mathbf{N}(\eta)^T \mathbf{f}(\xi,\eta) \xi |\mathbf{J}_b| \, \mathrm{d}\eta \, \mathrm{d}\xi, \tag{68}$$

which is solved using numerical integration.

As well as in stiffness matrix computation, the body forces vector can be divided into boundary and domain contributions

$$\mathbf{f} = \begin{Bmatrix} \mathbf{f}^{sb} \\ \mathbf{f}^{0} \end{Bmatrix}, \tag{69}$$

where $\mathbf{f}^{sb}$ is the vector that computes the contribution of the body loads vector on the boundary, and $\mathbf{f}^0$ is the body forces vector computed with bubble functions.

5 Results

5.1 Steklov problem

Firstly it is evaluated the approximation of a singular scalar problem with SBFEM. Such a problem has no body loads.

The Laplace equation on a circular domain has the analytic solution expressed as in Eq. 70 with boundary conditions given by Eqs. 71 and 72. This example was chosen because it contains fractional powers of r. If this problem would be approximated with traditional finite elements (FEs), one would expect a rate of convergence for the energy norm of 2/3, regardless of the polynomial order of approximation.

$$u(r,\theta) = \Sigma_{i=1}^{i=6} \frac{11-i}{45} r^{\frac{2}{3}i} \cos\left(\frac{2}{3} i\theta\right) \quad 0 \le r \le 1 \;\; 0 \le \theta \le \frac{3}{2}\pi \tag{70}$$

$$u(1,0) = 1 \tag{71}$$

$$\left.\frac{\partial u}{\partial n}\right|_{r=1} = \lambda_i u(r,\theta). \tag{72}$$

where $\lambda_i = \frac{2}{3} i$.

Figure 4 shows a mesh of 4 refinement steps and its respective solution for u, using a polynomial approximation equal to 8, post-processed on Paraview. For this case, the norm of the error was equal to 4.75E-12 for L^2 norm- almost the analytical solution.

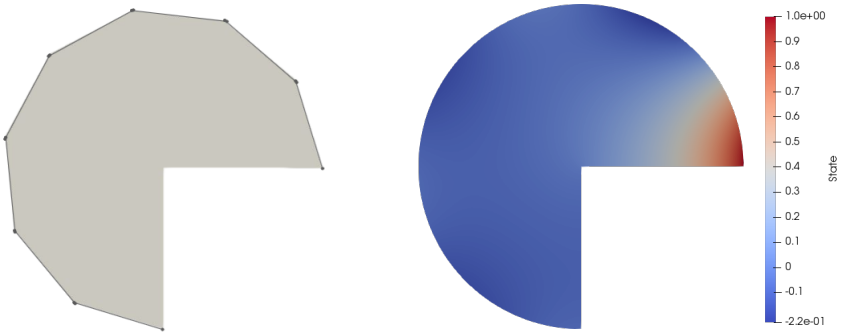

Figure 4. SBFEM mesh and post-processing solution for polynomial order equal to 8.

Table 2 summarizes the error values, from the polynomial order of 2 to 8. It is observed that the rate of convergence is equal to p and $p+1$ for energy norm and L^2 norm, respectively, where p is the polynomial order.

Table 2. Convergence of Steklov eigenvalues.

p	**h**	**n. equations**	**Error Energy**	**Error L^2**	**Error div**	**Conv. - Energy**	**Conv - L^2**
2	0.524	5	8.30E-01	5.83E-01	5.90E-01		
	0.262	9	3.17E-01	1.37E-01	2.86E-01	1.3886	2.0871
	0.131	17	6.87E-02	1.35E-02	6.73E-02	2.2061	3.3510
	0.0654	33	1.73E-02	1.03E-03	1.73E-02	1.9852	3.6927
	0.0327249	65	4.33E-03	9.56E-05	4.33E-03	2.0003	3.4405
	0.01636245	129	1.08E-03	1.10E-05	1.08E-03	1.9992	3.1145
3	0.524	7	4.96E-01	2.51E-01	3.04E-01		
	0.262	13	7.48E-02	1.05E-02	7.40E-02	2.7292	4.5809
	0.131	25	1.19E-02	9.99E-04	1.19E-02	2.6521	3.3917
	0.0654	49	1.53E-03	5.71E-05	1.53E-03	2.9528	4.1192
	0.0327249	97	1.92E-04	2.99E-06	1.92E-04	2.9963	4.2597
	0.01636245	193	2.41E-05	1.72E-07	2.41E-05	2.9978	4.1215
4	0.524	9	2.48E-01	5.85E-02	2.41E-01		
	0.262	17	2.50E-02	4.33E-03	2.47E-02	3.3103	3.7571
	0.131	33	1.64E-03	9.76E-05	1.64E-03	3.9302	5.4706
	0.0654	65	1.06E-04	2.34E-06	1.06E-04	3.9429	5.3737
	0.0327	129	6.64E-06	7.02E-08	6.64E-06	3.9961	5.0557
5	0.524	11	8.56E-02	2.77E-02	8.10E-02		
	0.262	21	5.19E-03	4.16E-04	5.18E-03	4.0438	6.0559
	0.131	41	1.86E-04	7.01E-06	1.86E-04	4.8024	5.8906
	0.0654	81	5.97E-06	1.09E-07	5.97E-06	4.9505	5.9909
6	0.524	13	5.41E-02	8.85E-03	5.34E-02		
	0.262	25	1.04E-03	8.56E-05	1.04E-03	5.7010	6.6924
	0.131	49	1.78E-05	5.78E-07	1.78E-05	5.8686	7.2110
	0.0654	97	2.85E-07	4.17E-09	2.85E-07	5.9517	7.0995
7	0.524	15	8.19E-03	1.54E-03	8.04E-03		
	0.262	29	1.71E-04	9.18E-06	1.70E-04	5.5818	7.3923
	0.131	57	1.47E-06	3.77E-08	1.47E-06	6.8620	7.9261
	0.0654	113	1.18E-08	1.50E-10	1.18E-08	6.9456	7.9540
8	0.524	17	5.96E-03	6.56E-04	5.93E-03		
	0.262	33	2.52E-05	1.30E-06	2.52E-05	7.8857	8.9790
	0.131	65	1.07E-07	2.48E-09	1.07E-07	7.8797	9.0359
	0.0654	129	4.29E-10	4.75E-12	4.29E-10	7.9449	9.0064

The problem was approximated with only one SBFEM element composed of $2^i; 0 \leq i \leq 4$ skeleton elements and polynomial order of approximation $2 \leq p \leq 8$. Figure 5 shows the rate of convergence for the energy and L^2 norm as a function of the element size for a given order of approximation. In all cases, optimal orders of approximation were obtained even though the solution contains fractional orders of r.

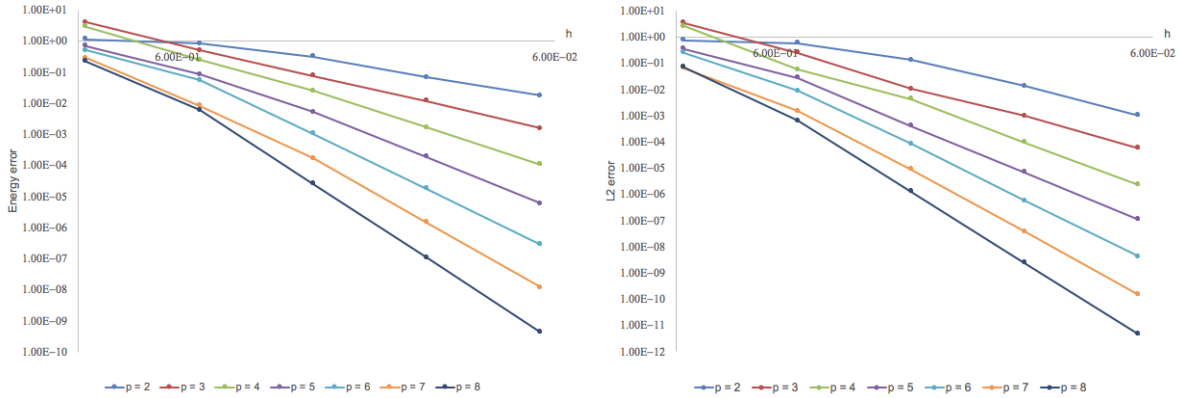

Figure 5. Rate of convergences for a singular problem as a function of h.

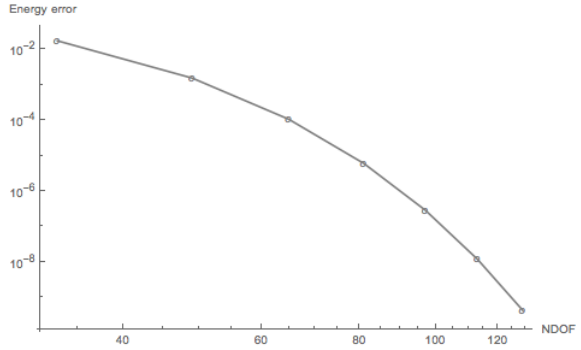

Figure 6. Rate of convergence for a mesh with numbers of skeletons equal to 16, as a function of p.

Figure 6 illustrates that SBFEM yields exponential rates of convergence even for singular problems. The curve corresponds to a 4 times of h-refinements of the skeleton elements (the number of skeleton elements equal to 16).

Approximation of a singular scalar problem with SBFEM

In the case where the geometry of the skeleton element is a circle with the scaling center at the center of the circle, the SBFEM eigenvalues will converge to the Steklov eigenvalues. The Steklov eigenvalues of an elliptic problem are defined as finding the function u_i, λ_i pairs such that

$$\begin{aligned} -\Delta u_i(x) &= 0 \quad x \in \Omega \\ \frac{\partial u_i(s)}{\partial n} &= \lambda_i u_i(s) \quad s \in \partial\Omega. \end{aligned} \tag{73}$$

In the case of SBFEM, there may be parts of the domain where homogeneous Neumann conditions are satisfied:

$$\begin{aligned} -\Delta u_i(x) &= 0 \quad x \in \Omega \\ \frac{\partial u_i(s)}{\partial n} &= \lambda_i u_i(s) \quad s \in \partial\Omega_E \\ \frac{\partial u_i(s)}{\partial n} &= 0 \quad s \in \partial\Omega_I, \end{aligned} \tag{74}$$

where the subindex E stands for external and I stands for internal.

In the case of the domain depicted in Fig. 4, the Steklov eigenvalues are equal to $\lambda_i = 2i/3$ and the eigenvectors are $u(r,\theta) = r^{2i/3}\cos(\frac{2i}{3}\theta)$. For the solution with 4 skeleton elements (the coarsest configuration that converges uniformly in p) we map the eigenvalues of the SBFEM element for different values of polynomial order p are shown in Table 3. Thus, it can be seen that the SBFEM eigenvalues converges to the Steklov eigenvalues increasing the polynomial order.

Table 3. Convergence of Steklov eigenvalues.

p/λ_i	2/3	4/3	2	8/3	10/3	4	14/3	16/3	6	20/3	22/3
p=2	0.666837	1.33834	2.03303	2.94042	3.72574	4.81523	5.98255	6.57498	-	-	-
p=3	0.666667	1.33342	2.00139	2.66741	3.36969	4.10531	4.90051	6.57498	7.41283	8.86774	10.3652
p=4	0.666667	1.33333	2.00003	2.66741	3.33576	4.01036	4.69954	5.35265	6.21089	7.07151	7.99644
p=5	0.666667	1.33333	2	2.66667	3.33344	4.00065	4.66961	5.35265	6.02985	6.73883	7.48237
p=6	0.666667	1.33333	2	2.66667	3.33334	4.00003	4.66684	5.33342	6.00309	6.67625	7.35854
p=7	0.666667	1.33333	2	2.66667	3.33333	4	4.66667	5.33342	6.00023	6.66757	-7.33633
p=8	0.666667	1.33333	2	2.66667	3.33333	4	4.66667	5.33333	6.00001	6.66673	7.33359

5.2 Poisson problem

The first example with body loads is a Poisson problem whose solution is given by:

$$u(x,y) = \cos\frac{\pi x}{2}\cos\frac{\pi y}{2}. \tag{75}$$

which is a smooth bubble in a rectangular domain $\Omega = [-1;-1]\times[1;1]$. This example is evaluated using SBFEM and FEM. A comparison between both methods is accomplished.

Four refinement steps of h were evaluated for linear, quadratic and cubic polynomial order. The rate of convergence is p for energy and $p+1$ for L^2 norm. The convergence curves in the log-log scale are shown in Fig. 7. For this example, we compare the complete bubble functional space, with the functional space based only on the polynomial approximation (without the rational functions).

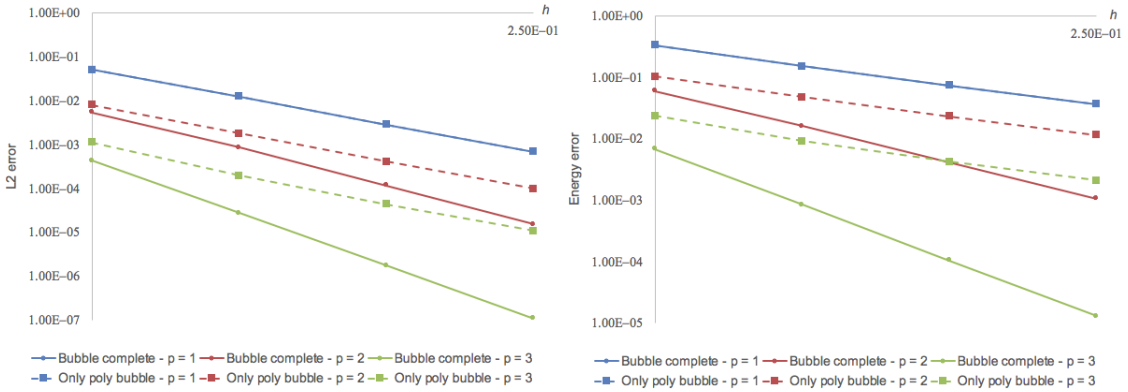

Figure 7. Poisson problem: SBFEM convergence curves for L^2 norm (left) and Energy norm (right).

Figure 7 illustrates that the rate of convergence of a polynomial bubble does not grow, even increasing the polynomial order of the approximation. Moreover, it leads to higher errors, except for the linear case. This is the only case in which the incomplete functional space does not leads to lower error values. It occurs because in such approximation the SBFEM leads to only integer eigenvalues, and then it will not be any effect of rational exponents on the bubble.

In the following, Table 4 shows the convergence values. The post-processing is presented in Fig. 8.

Table 4. Poisson problem: Errors and convergence ratios

p	h	N. equations	Error energy	Error L^2	Error div	Conv. - Energy	Conv. - L^2
1	2	5	0.825047	0.170247	0.825047		
	1	13	0.671313	0.106201	0.671313	0.2975	0.6808
	0.5	41	0.303937	0.0202969	0.303937	1.1432	2.3875
	0.25	145	0.147023	0.00507276	0.147023	1.0477	2.0004
2	2	20	0.266142	0.0345822	0.266142		
	1	69	0.122586	0.0128022	0.122586	1.1184	1.4336
	0.5	257	0.0328763	0.00184029	0.0328763	1.8987	2.7984
	0.25	993	0.00843641	0.000241642	0.00843641	1.9623	2.9290
3	2	41	0.0470566	0.00521883	0.0470566		
	1	149	0.0137393	0.000983065	0.0137393	1.7761	2.4084
	0.5	569	0.00166989	5.79E-05	0.00166989	3.0405	4.0844
	0.25	2225	0.000207039	3.56E-06	0.000207039	3.0118	4.0238

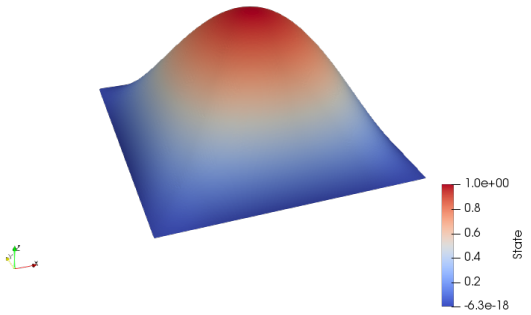

Figure 8. Poisson problem: Post-processed solution with SBFEM.

To compare the accuracy of SBFEM and its rates of convergence, the same problem was evaluated with FEM. In Table 5 it can be observed that the error norms are significantly higher than the ones obtained with SBFEM. However, the number of DOFs used in SBFEM is higher than FEM, due to the bubble functions added to the formulation.

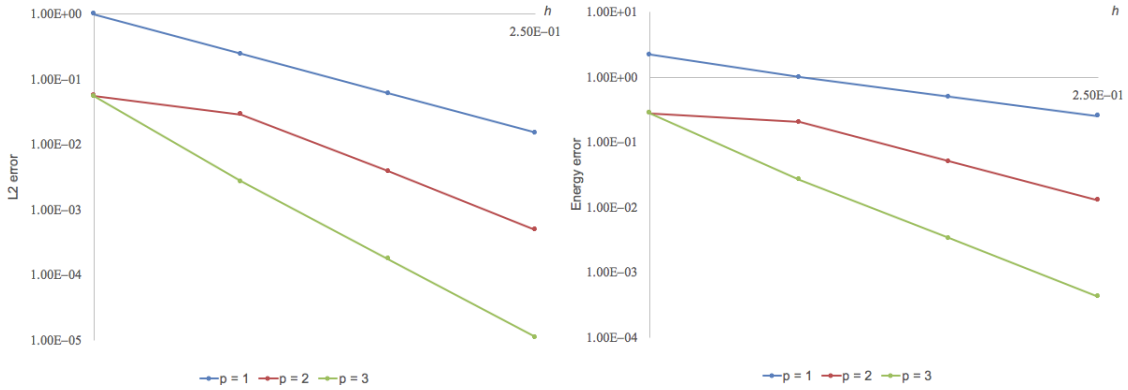

Figure 9. Poisson problem: Convergence curves for L^2 norm (left) and energy norm (right) for FEM.

Table 5. Poisson problem: Errors and rates of convergence

p	h	n. equations	Error Energy	Error L^2	Error div	Conv. rate Energy	Conv - L^2
1	2	4	2.22144	1	2.22144		
	1	9	0.996326	0.243587	0.996326	0.2604	0.4072
	0.5	25	0.501368	0.0607841	0.501368	0.9670	1.4787
	0.25	81	0.251514	0.015202	0.251514	0.8432	1.8390
2	2	9	0.280025	0.0553988	0.280025		
	1	25	0.202044	0.0288079	0.202044	0.8960	1.1416
	0.5	81	0.0509764	0.00386416	0.0509764	1.4528	2.3587
	0.25	289	0.012762	0.000490218	0.012762	1.8670	2.8019
3	2	16	0.280023	0.0552928	0.280023		
	1	49	0.0266822	0.00271882	0.0266822	0.7861	0.9506
	0.5	169	0.00337643	0.000176249	0.00337643	3.0358	4.0621
	0.25	625	0.00042331	1.11E-05	0.00042331	3.0000	4.0000

5.3 Elasticity Problem

The following examples were evaluated in [9], in which elasticity equation with non-zero body loads is represented by:

$$\text{Div}(\mathbf{S}) + \mathbf{b}_0 = \mathbf{0} \tag{76}$$

where $\mathbf{b}$ is the body load vector and $\mathbf{S}$ is the stress tensor for isotropic materials given by

$$\mathbf{S} = 2\mu\boldsymbol{\epsilon} + \lambda \text{tr}(\mathbf{E})\mathbf{I} \tag{77}$$

where λ and μ are the first and second Lamé parameters, equal to 1.0 and 0.3, respectively.

The domain in both cases is a square-shaped domain $\Omega = (0, 1)^2$, discretized with only quadrilateral meshes with four levels of refinement. The body loads are polynomial and are obtained substituting the solution given by Eq. 78 on Eq. 76.

$$\mathbf{u} = \begin{Bmatrix} x^2y^2(1-x)^3(1-y)^3 \\ x^2y^2(1-x)^3(1-y)^3 \end{Bmatrix} \tag{78}$$

For the convergence analysis, Fig. 10 shows rate of convergence $p+1$ for L^2 norm and p for energy norm, as well as shown on the Poisson examples. Table 6 summarizes the absolute values form error norm. It can be seen that good approximations were obtained and the error converges to zero as the polynomial order of approximation rises.

Table 6. Elasticity problem - Example 1: Errors and rates of convergence for FEM mesh.

p	h	n. equations	Error Energy	Error L^2	Error div	Conv. Energy	Conv. L^2
1	2	12	0.00349857	0.000260941	0.00224467		
	1	34	0.00292084	0.000196768	0.0020178	0.2	0.4
	0.5	114	0.00149425	7.06E-05	0.00122492	1.0	1.5
	0.25	418	0.000832876	1.97E-05	0.000695685	0.8	1.8
2	2	40	0.00206175	0.000107633	0.00149272		
	1	138	0.00110792	4.88E-05	0.000916829	0.9	1.1
	0.5	514	0.000404725	9.51E-06	0.000341002	1.5	2.4
	0.25	1986	0.000110956	1.36E-06	9.47E-05	1.9	2.8
3	2	84	0.000651673	2.39E-05	0.000472354		
	1	306	0.000377909	1.24E-05	0.000318266	0.8	1.0
	0.5	1170	4.61E-05	7.42E-07	3.93E-05	3.0	4.1
	0.25	4578	5.88E-06	4.58E-08	5.02E-06	3.0	4.0

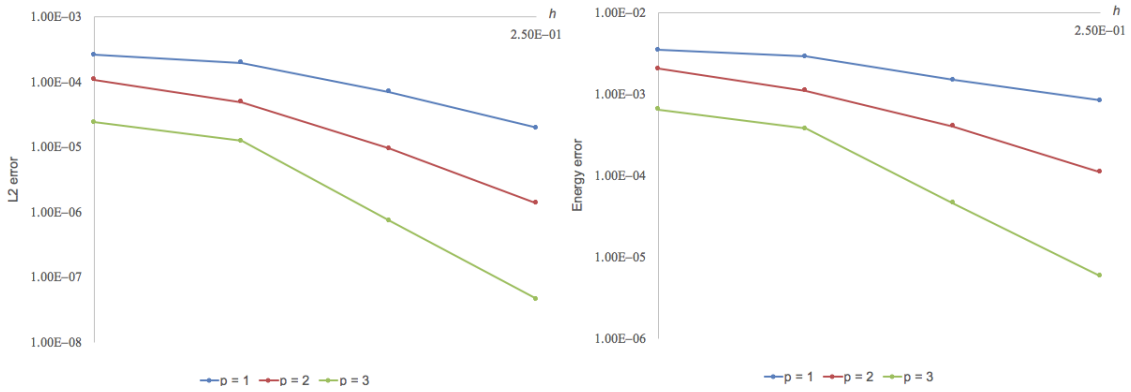

Figure 10. Elasticity problem - Example 1: Convergence curves for L^2 norm (left) and energy norm (right).

Figure 11 shows strain ϵ_x obtained from the 2×2 mesh using the bubble function approach for body loads with cubic elements. This result is very similar to the solution presented by Ooi and coauthors [9]. Therefore, bubble functions can lead to good approximations even with coarse meshes.

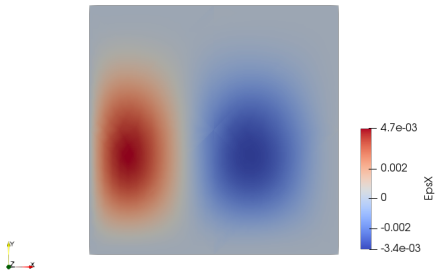

Figure 11. Post-processed solution for ϵ_x with SBFEM for order equal to 3.

6 Conclusions

The SBFEM approach is enhanced with a procedure for constructing a bubble functional space. Such a space is based on bubble functions that are orthogonal to the SBFEM functions. Due to the orthogonality, the formulation can be divided into a domain and boundary problem, which can reduce the computational cost of the SBFEM simulations. Moreover, some properties of the collapsed FEM are applied for computation of the SBFEM coefficient matrices. These strategies were implemented in an object-oriented FE library, which was expanded to accomplish simulations with SBFEM. Optimum rates of convergence were obtained even for problems with square-root singularity. Furthermore, Poisson and Elasticity examples were compared to FEM traditional approach, indicating the accuracy of the SBFEM simulation with bubble functions.

Acknowledgements

The authors thankfully acknowledge financial support from FAPESP (São Paulo Research Foundation) grant 2014/05155-0, and ANP (Brazilian National Agency of Petroleum, Natural Gas and Biofuels), grant 2014/00090-2.

References

[1] Wolf, J. P., 2003. *The scaled boundary finite element method*. John Wiley & Sons.

[2] Song, C., 2018. *The Scaled Boundary Finite Element Method: Theory and Implementation*. John Wiley & Sons.

[3] Yang, Z., Deeks, A., & Hao, H., 2007. Transient dynamic fracture analysis using scaled boundary finite element method: a frequency-domain approach. *Engineering Fracture Mechanics*, vol. 74, n. 5, pp. 669–687.

[4] Bazyar, M. H. & Song, C., 2006. Time-harmonic response of non-homogeneous elastic unbounded domains using the scaled boundary finite-element method. *Earthquake engineering & structural dynamics*, vol. 35, n. 3, pp. 357–383.

[5] Song, C., 2006. Analysis of singular stress fields at multi-material corners under thermal loading. *International journal for numerical methods in engineering*, vol. 65, n. 5, pp. 620–652.

[6] Chiong, I., Ooi, E. T., Song, C., & Tin-Loi, F., 2014. Scaled boundary polygons with application to fracture analysis of functionally graded materials. *International Journal for Numerical Methods in Engineering*, vol. 98, n. 8, pp. 562–589.

[7] Wu, Y.-L., 1993. Collapsed isoparametric element as a singular element for a crack normal to the bi-material interface. *Computers & structures*, vol. 47, n. 6, pp. 939–943.

[8] Boffi, D., Brezzi, F., Fortin, M., et al., 2013. *Mixed finite element methods and applications*, volume 44. Springer.

[9] Ooi, E. T., Song, C., & Natarajan, S., 2016. Construction of high-order complete scaled boundary shape functions over arbitrary polygons with bubble functions. *International Journal for Numerical Methods in Engineering*, vol. 108, n. 9, pp. 1086–1120.

[10] Ooi, E., Song, C., & Natarajan, S., 2017. A scaled boundary finite element formulation with bubble functions for elasto-static analyses of functionally graded materials. *Computational Mechanics*, vol. 60, n. 6, pp. 943–967.